Spin transport and superconductivity in half-metallic nanowires and junctions

Yao, J.

6

Inducing Triplet Supercurrent in Long Half-metallic Ferromagnets

Superconducting junctions with a ferromagnet as the weak link, where triplet correlations can transport over a substantial distance, have been reported theoretically and experimentally. Next to the research on CrO_2-based junctions, triplets were also found in manganite oxides, i.e., $La_{0.7}Ca_{0.3}MnO_3$ (LCMO) and $La_{0.7}Sr_{0.3}MnO_3$ (LSMO), in combination with high-T_c superconductor $YBa_2Cu_3O_7$ (YBCO). However, many questions are still open, and in particular the generation mechanism of triplets is not clear yet in these systems. In this work, we study the triplet transport in a lateral configuration of LSMO nanowire junctions with NbTi superconducting contacts. By varying either the width or the length of the LSMO nanowires, we observe superconducting (critical) currents, and distinguishing superconducting quantum interference (SQI) patterns when sweeping a magnetic field $B_\perp$ perpendicular to the plane of the wire. This clearly points to diffusive transport of triplets in these LSMO-based junctions. The research demonstrates that combinations of oxide magnets with conventional (s-wave) alloy superconductors can be a promising new route to realizing superconducting spintronics.

This chapter is in preparation for publication.

6.1. Introduction

Long-range proximity (LRP) effects in the superconductor/half-metallic ferromagnet (S/HMF) hybrids, in which conventional spinless singlets are converted to odd-frequency spinfull triplets that can exist up to micrometric distance in HMFs, have been reported previously [14, 69, 70]. Unlike conventional ferromagnets (F), HMFs are nearly 100% spin-polarized. Therefore, the equal-spin triplets ($S = \pm 1$) are not susceptible to the pair-breaking exchange field in HMFs, while opposite-spin singlets ($S = 0$) can hardly exist, giving rise to a significant difference in coherence length ξ for both types of pairs. There are only a few HMF materials. One example is CrO_2. In combination with alloy superconductors, triplets were generated in CrO_2-based hybrids via magnetic inhomogeneity established either by strain or disorder of grain boundaries [167]. Moreover, colossal spin valve effects and high-density critical supercurrents were observed using stacked S/F/CrO_2 geometries [71, 74, 183]. Similarly, the LRP effect was studied in high-T_c YBCO/LCMO and YBCO/LSMO systems [14, 73]. Visani, *et al.* reported equal-spin Andreev reflections at the interface between YBCO and LCMO in a vertical architecture, and the existence of triplets in the LCMO layer of 30 nm [73]. Interestingly, uncompensated magnetic moments were discovered at the Cu-O-Mn chains across the interface between YBCO and LCMO that could be a source of magnetic inhomogeneity, although the relation to triplet generation was not elucidated [184]. Very recently, extremely long coherent transport of triplets was found in lateral YBCO/LSMO/YBCO junctions [14]. Sanchez-Manzano, *et al.* observed LRP effects in quite wide (20 or 25 μm) but also quite long (1 μm) LSMO wires, where multiple magnetic domain walls were present and possibly played a role in triplet generation and transport. Despite the LRP effect being unequivocally observed in the high-T_c S/HMF systems, the underlying physics, in particular with respect to the triplet generation, still remains to be explored.

In Chapter 5, we showed the generation and transport of triplets in NbTi/LSMO junctions of small length (20 nm) and shaped as disks, squares and bars by Focused Ion Beam etching. Triplets were found in all of them. In the bar-shaped junctions (aspect ratios of 3:1 and 5:1) typical Fraunhofe-liker patterns were obtained by examining the SQI response when applying perpendicular magnetic fields $B_\perp$ fields. Given the strong shape anisotropy, any form of spin texture was believed to be absent in the bar-shaped junctions. Therefore, we suspect the origin of triplets generation arises from the intrinsic magnetic inhomogeneity of the LSMO layer. In this Chapter we take that idea further, and fabricate (much) longer junctions, using e-beam lithography and a hard-mask techique, still on the basis of LSMO and NbTi. We find that supercurrents can be induced over exceptionally long lengths, up to 1.3 μm, with appreciable current densities.

6.2. Device Fabrication

The first part of this section describes the fabrication of the lateral junctions using a Pt hard mask technique. The second part gives some details about opening the etch step that removes the NbTi and forms a junction with LSMO only. More details, in particular about etching rates for the various materials, are given in Appendix 6.5.

Nanofabrication of long NbTi/LSMO junctions

We fabricated a number of nanowire NbTi/LSMO junctions with different widths and lengths. Starting point for the fabrication is still a NbTi/LSMO bilayer, similar to Chapter 5. Instead of using a focused ion beam to define the junction, here we developed a method involving a hard mask to structure the bilayer, as schematically depicted in Fig. 6.1. The LSMO thin film (40 nm) was grown as before, on a (001)-oriented LSAT crystal substrate at 700 ^oC in an off-axis sputtering system. The deposition pressure was kept at 0.7 mbar by flowing a mix of Argon and Oxygen gas (3:2). The sputtering power was 50 W. Cooling down the system to room temperature started at 25 ^oC/min, but we waited several hours to reach a low temperature and minimize possible issues with interdiffusion. Then the system was pumped down to 10^{-7} mbar, followed by the sputter deposition of NbTi (60 nm) on the LSMO layer $in\ situ$, in an Ar atmosphere with a pressure of 0.1 mbar. Note that the vacuum is not broken in this step, which is vital for creating a clean interface and thus generating triplets effectively, as already seen in Chapter 5. Next, a positive e-beam resist was spin-coated on the NbTi/LSMO bilayer and a pattern was written by exposure to an electron beam (Fig. 6.1I, II). We advisedly did not use a negative resist mask, where the desired structure is left standing, in combination with direct Argon etching. The etch rate of resists is high in ion beam etching (IBE) and the resist mask will be removed completely before succeeding to pattern the NbTi/LSMO bilayer. Therefore, the sample with the patterned resist layers was loaded into an on-axis radio-frequency sputtering system and a thick Pt layer (425.8 nm) was deposited. The choice for Pt, and for the thickness of 425.8 nm, is explained in the Appendix 6.5. After lifting off, the Pt served as a hard mask protecting the NbTi/LSMO bilayer (Fig. 6.1III). In the next step, shown in Fig. 6.1IV, the NbTi/LSMO bilayer was patterned. In this step, ideally, the Pt layer is fully removed, but the bilayer should be intact. To open up a gap and form a junction, *i.e.* making LSMO the weak link, the NbTi needs to be removed. For this we repeated the above procedure with Pt liftoff. The only difference in this step was that the central part of the nanowire was uncovered by the Pt hard mask and hence removed by IBE (Fig. 6.1V). In this way, we obtained well-defined lateral NbTi/LSMO/NbTi junctions with adjustable widths and lengths (Fig. 6.1VI). A series of devices were produced, which we call Dvn, with n the device number. Their length, width, and basic parameters are collected in Table 6.1. In the coming discussion, we will regularly refer to these different devices.

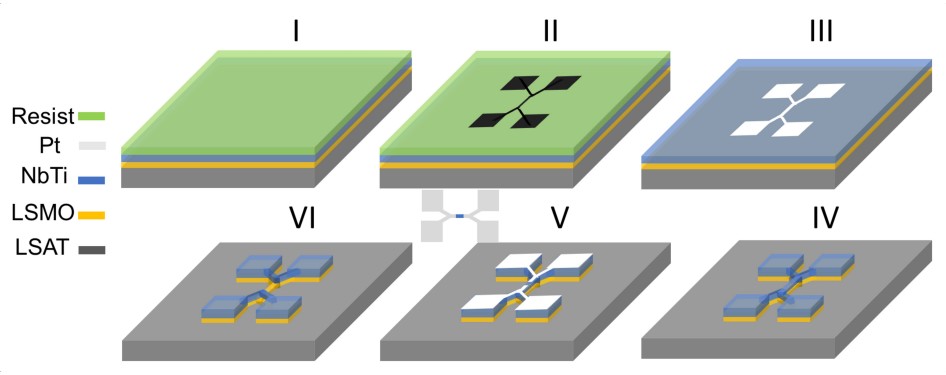

Figure 6.1: Illustrative scheme of the nanofabrication procedure of NbTi/LSMO junctions. I: A positive resist is coated on NbTi/LSMO bilayer. II: The desired pattern is written in the positive resist by electron beam lithography (EBL). III: Pt is deposited and becomes a mask after removing the positive resist. IV: NbTi/LSMO bilayer is patterned by ion beam etching (IBE) with a Pt mask. Note that, ideally, the Pt mask should be removed completely in this step. V: Repeating steps I to III, a Pt mask is made again to further structure the patterned NbTi/LSMO bilayer by leaving the central region uncovered (see the small sketch with top view; the blue part is the uncovered region). VI: The NbTi/LSMO/NbTi lateral junction is fabricated by employing IBE, and the central region is an LSMO (yellow) nanowire without NbTi on top.

Details of the weak link fabrication

Several etch steps in the procedure depend crucially on the etch rate for the different materials. These were collected in a series of accurate measurements on films of the relevant materials, involving thickness measurements by small-angle x-ray diffraction and Atomic Force Microscopy. Numbers can be found in Appendix 6.5. Also, the resistivity of LSMO was characterized for different wire widths and lengths. Although this could be supposed to be a material parameter, in particular, different widths consistently gave somewhat different numbers for ρ, and knowing such actual values was of use in finding the proper etch procedures. Below we show an example of data from the

Junctions	l(nm)	$w(\mu$m)	$R_N(\Omega)$	T_c(K)
Dv2	678	1.912	20	<0.4
Dv3	586	2.04	20	5.19
Dv4	1349	5.12	6	6.4
Dv5	756	4.89	4.6	6.4
Dv6	640	5.13	4.9	5.78
Dv10	1126	3.52	-	-

Table 6.1: Overview of the NbTi/LSMO junctions with varying widths and lengths. The length and width are directly measured by scanning electron microscopy. It should be noted the R_N of the lateral NbTi/LSMO junction can not be precisely determined as the superconducting transition window is wide. Here, we take the rough value to evaluate the etching process referring to the calculated R. T_c is extracted from the RT measurement with a criterion of 0.2 Ω.

last step in the junction fabrication when the NbTi (60 nm) is etched away. Too little etching leaves an unwanted superconductor, and too much etching very quickly affects the LSMO (40 nm). To determine when the etching has cut through the NbTi layer, we measured the temperature-dependent resistance (RT) of the selected device Dv5 after different consecutive etch steps. The length of the gap, that is the length of the junction, and the width of the central nanowire of Dv5 are determined to be 4.887 μm and 755.6 nm by scanning electron microscopy (SEM) (Fig. 6.2a). The RT data after a first, second, and third etch step are shown in Fig. 6.2. We observe the well-known signature of a proximized structure, where the banks become superconducting first, followed by a plateau that is determined by the resistance of the weak link, and then a resistance drop to zero temperature if the link becomes fully superconducting. The first drop is seen around 6.9 K, the second one around 6.5 K to 4.5 K. We can approximately calculate the (expected) resistance of Dv5 in case the weak link consists of LSMO. According to $R = \rho l/S$, where ρ for this device is taken to be ≈ 100 $\mu\Omega$cm, l is the length, and S is the cross section, we obtain $R_5 \approx 3.9$ Ω. The measured resistance of Dv5 is in good agreement with the calculated value after the first and second etching (Fig. 6.2b and c). However, the resistance of Dv5 becomes almost 8 times larger after the third etching (Fig. 6.2d), indicating the LSMO layer is over-etched. Since IBE is utilized to remove the unwanted NbTi layer, it may also contaminate the LSMO layer if the etching time is not optimized, leading to a pronounced increase in resistance, as verified in Fig. 6.2d. Therefore, we take the recipe of the second etching to make the NbTi/LSMO junctions to ensure the NbTi is completely removed, and LSMO is slightly etched to form a ferromagnetic weak link.

Furthermore, we employed energy-dispersive X-ray spectroscopy (EDX) to qualitatively examine the NbTi/LSMO junctions fabricated using the optimal recipe. For this, we used Dv10 and mapped the elements Pt and Nb. The width of Dv10 is 3.523 μm, and the length is about 1.126 μm (Fig. 6.3a). These dimensions facilitate the EDX analyses. As shown in Fig. 6.3b, the Pt hard mask was not destroyed after the optimal etching. However, Nb was absent (Fig. 6.3d), in contrast to a relatively strong EDX intensity of Nb before etching (Fig. 6.3c), indicating NbTi was removed in the gap region. Therefore, we conclude we are able to make long LSMO-based junctions using the recipe introduced above. The electrical transport measurements, to be discussed next, lead to a similar conclusion.

6.3. Characterization by transport measurements

Having fabricated a series of nanowire NbTi/LSMO junctions, we performed transport measurements on these junctions with temperature and field sweeps, yielding RT and SQI characterizations. We first discuss the devices Dv2 and Dv3 that have a similar width of about 2 μm (see Table 6.1), followed by Dv4 and Dv6, also of similar width,

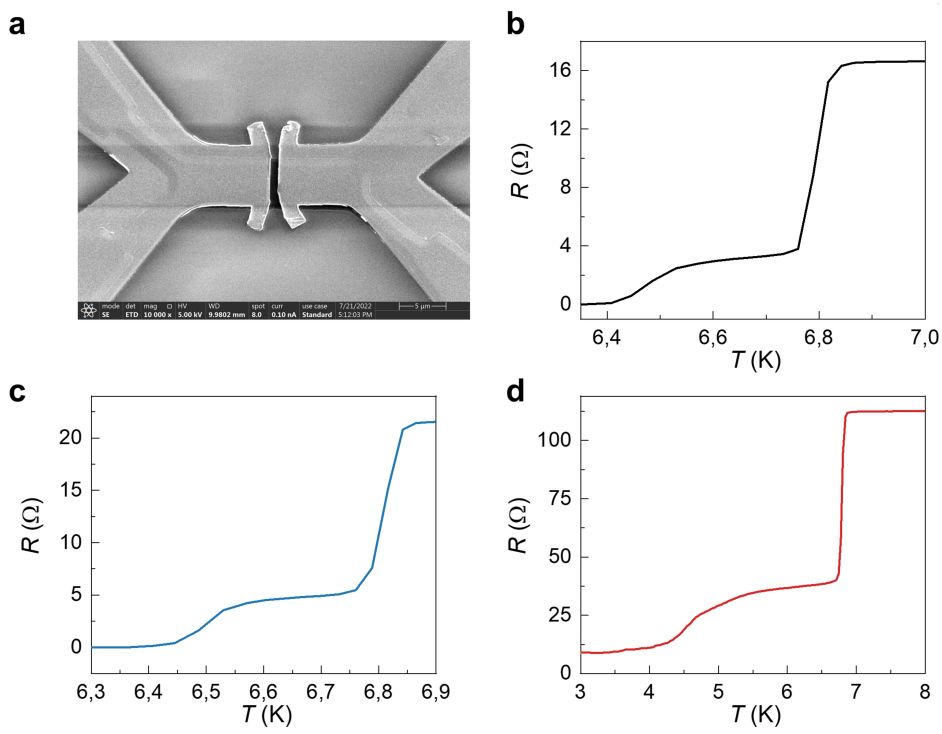

Figure 6.2: Electrical characterizations on Dv5. (a) Top-view SEM image of Dv5. RT measurements of Dv5 after first etching (b), second etching (c), and third etching (d), respectively. Note during the etching procedure, only the central uncovered NbTi was removed, and the rest were protected by the Pt capping layer.

but larger (about 5 μm).

Devices with smaller width, 2 μm

As shown in Fig. 6.4a, the dimension of Dv3 is 2.04 μm wide (w) and 586 nm long (l). The measured ρ of a LSMO nanowire of this width is about 200 $\mu\Omega$cm. Therefore, we calculate $R_3 \approx 14.4\ \Omega$. The resistance of Dv3 was measured with decreasing temperature in a quasi-four-probe configuration (see Fig. 6.4b). Below 7 K, the transition temperature of the NbTi, R of Dv3 is about 20 Ω and gradually decreases, reaching zero at around 4.8 K. The measured resistance in the plateau is 40% higher than the calculated value, indicating that the LSMO may be slightly over-etched. The broad tail of the RT curve is attributed to the onset of the proximity effect in the weak link and seen in every measured junction in this work. Therefore, we define the temperature transition window (TTW), that is, the width of the tail, as a reference to compare junctions with different dimensions. The zero-voltage state of current versus voltage (IV) curves is displayed in the inset of Fig. 6.4b, and clearly shows the signature of a superconducting junctions. Once the applied current exceeds the critical current (I_c), the voltage

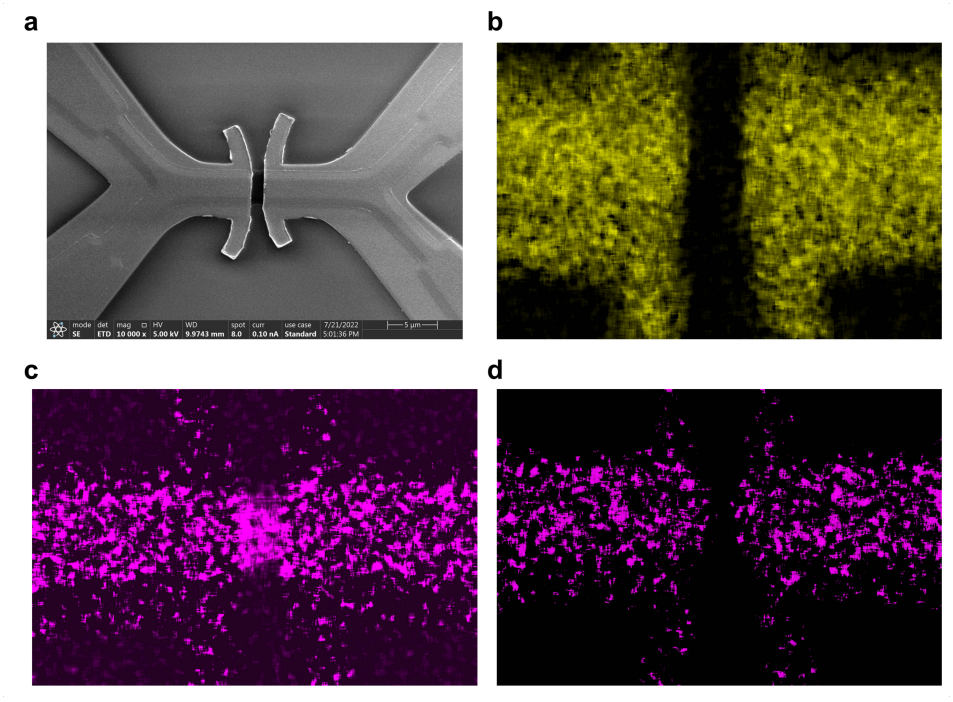

Figure 6.3: EDX analyses of Dv10. (a) Top-view SEM image of Dv10. (b) EDX image of the Pt hard mask. (c) EDX image of Nb before etching, and (d) EDX image of Nb after the optimal etching, demonstrating the absence of Nb in the gap.

increases abruptly as the induced superconductivity is destroyed.

We examined the SQI pattern of Dv3 by applying a magnetic field $B_\perp$, perpendicular to the junction plane, at 4.5 K (Fig. 6.4c). The measured pattern is far from the typical Fraunhofer-like pattern collected, for instance, on the bar-shaped NbTi/LSMO junctions shown in Chapter 5. Instead, it is quasi-Gaussian-like with a rather sharp decay of $I_c(B)$ up to 15 mT. If we ignore the shielding currents in the side NbTi arms, the first minimum for the Fraunhofer pattern would be expected at $\Delta B = \Phi_0/(wL)$. Taking L = 586 nm, this yields $\Delta B \approx 1.7$ mT. Clearly, the measured central peak of the SQI pattern is much wider. Note that the mean free path of LSMO (ℓ_H) is about 6.5 nm, and the coherence length (ξ_{HMF}) is calculated to be 19 nm. Given the length of Dv3 of about 586 nm, the case we deal with, for the triplet transport, is that of a diffusive long junction ($\ell_H \ll \xi_{HMF} \ll l$). That can lead to a Gaussian-shaped curve of the form $I_c(B)/I_c(0) = e^{-\Phi^2/(2\sigma^2\Phi_0^2)}$ under the condition that $L/w \gg 1$ [68, 185, 186]. Here Φ is the total flux threading the junction, σ is the geometry-dependent constant, and Φ_0 is the quantum flux. The problem is that for Dv3, $L/w \approx 0.3$, which should lead to a Fraunhofer pattern. Here we have to remember that we are dealing with a magnetic film with internal magnetic fields. The phase accumulation along paths, *i.e.* along the

width or along the length of the wire may well be different. There is no theory available yet to address this point.

Finally, we extracted $J_c(T)$ of Dv3 from the temperature-dependent IV measurements by taking a criterion of 0.2 Ω (Fig. 6.4d). At the base temperature of our cryostat (1.5 K), J_c is about 5×10^8 A/m^2, which is 1-2 orders of magnitude smaller than the value for NbTi.

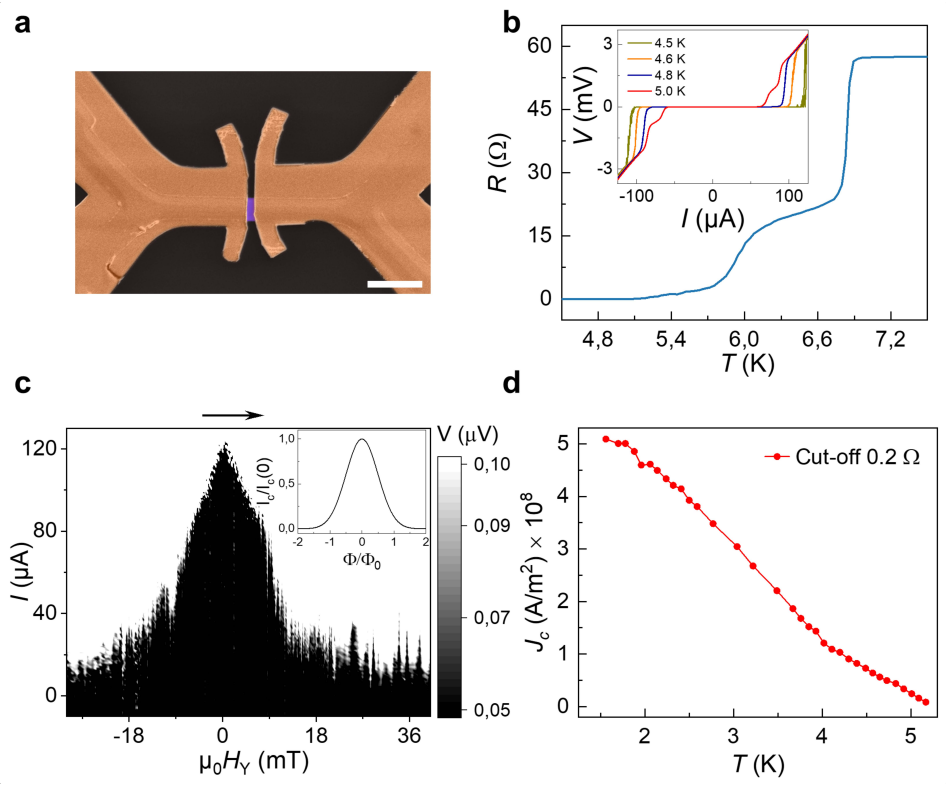

Figure 6.4: Ellectrical transport characterization of Dv3. (a) False-colored SEM image of Dv3. The scale bar is 5 μm. (b) A plot of the RT curve showing two transitions. Inset: IV curves at different temperatures. (c) SQI pattern measured at 4.5 K by sweeping $B_\perp$. (y is perpendicular to the junction out of plane). The arrow represents the field sweep direction. Inset: a plot of a simulated Gaussian-like SQI pattern. (d) The plot of the temperature-dependent critical current density J_c, extracted by taking a 0.2 Ω criterion.

Subsequently, we examined Dv2, which has similar dimensions as Dv3 and was grown in the same batch. The length and width of Dv2 are 1.91 μm and 0.68 μm (Fig. 6.5a), respectively. Although Dv2 is only slightly longer than Dv3, it exhibits significantly different behavior. As shown in Fig. 6.5b, the RT curve of Dv2 has a drop below 7 K, similar to the one observed in Dv3. However, instead of decreasing to zero, R remains almost constant down to 1.5 K. We then cooled down Dv2 further, with a ^{3}He insert reaching 0.4 K. Note that the temperature between 1.5 K and 1.35 K was not cal-

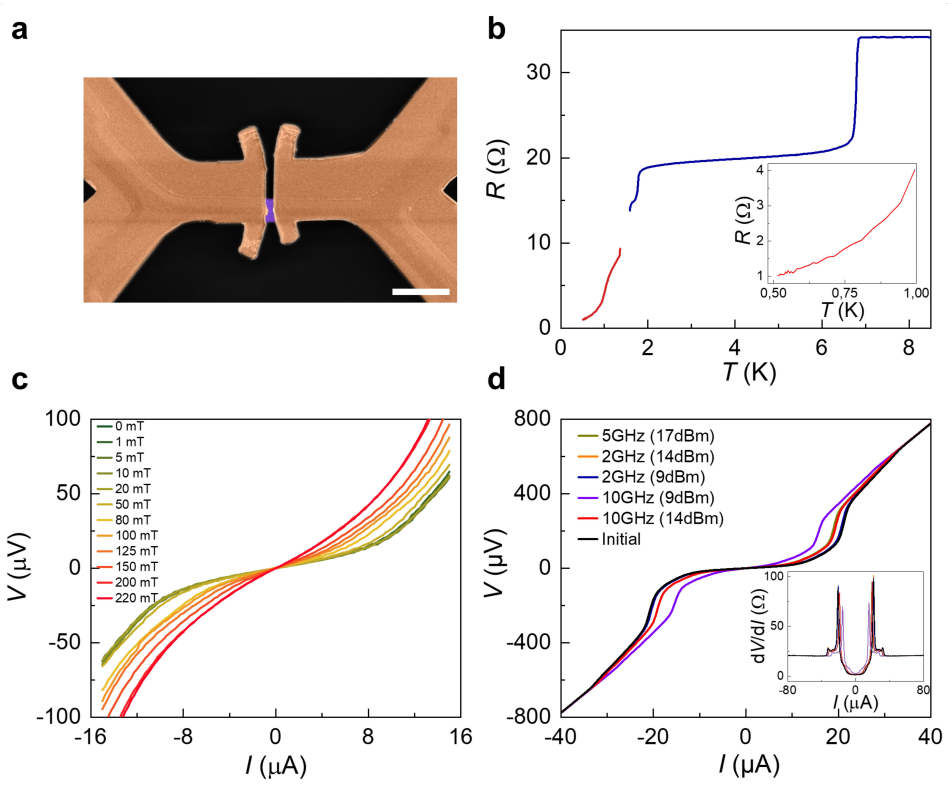

Figure 6.5: Electrical transport characterization of Dv2. (a) False-colored SEM image of Dv2. The scale bar is 5 μm. (b) A plot of the RT curve, in which the temperature was not calibrated between 1.5 K and 1.35 K. Inset: Magnification of the RT curve in the low-temperature region. (c) Plots of IVs at various $B_\perp$ measured at 0.4 K. (d) IV curves obtained under microwave excitation at 0.4 K, and the corresponding dV/dI plots (inset).

ibrated. At 0.5 K, Dv2 still has a residual resistance of 1 Ω (inset in Fig. 6.5b). Reaching 0.4 K, the resistance of Dv2 is about 0.7 Ω. If we again take $\rho \approx 200$ $\mu\Omega$cm, R_2 is calculated to be 17.7 Ω. The measured normal resistance of Dv2 is about 20 Ω, indicating Dv2 is also slightly over-etched as expected. Therefore, considering that the resistance of Dv2 decreases from 20 Ω to 0.7 Ω, and that the length of Dv2 is 678 nm, we conclude that approximately 95% of the weak link is proximized.

Since Dv2 is not fully proximized, the residual resistance prohibits a proper inspection of the SQI pattern. We hence performed IV measurements at different magnetic fields ($B_\perp$). At 0.4 K, IV curves were collected and plotted in Fig. 6.5c. Despite that I_c cannot be determined unambiguously in this case, the trend in the shapes suggests a monotonic decrease of I_c. Notably, the IV curve becomes nearly linear at 220 mT. We want to stress that the critical field of NbTi should be much higher (of the order of ten of Tesla) at 0.4 K, meaning there is no suspicion of NbTi shorts in Dv2. Given

the incompletely proximized Dv2, Josephson coupling cannot be proved. Alternatively, macroscopic phase coherence can be detected by Shapiro step measurements [48]. In a Josephson junction, the wavefunctions of the side superconductors overlap in the weak link, leading to a current-phase relation $I = I_0 \sin(\varphi)$, where $\mathrm{d}\varphi/\mathrm{d}t = 2\pi V/\Phi_0$, I_0 is the equilibrium critical current. In the presence of an ac voltage source, we obtain a dc response for $V = n\Phi_0 f/2\pi$, which yields an ohmic dependence with sharp spikes in the IV characteristics. f is the frequency of the external ac source. Therefore, we illuminated Dv2 by using a microwave source at different powers and frequencies. The results are plotted in Fig. 6.5d. Unfortunately, we failed to catch quantized steps in the IV measurements. Summarizing, one device in this batch shows all signs of the LSMO bridge being proximized over its full length of about 600 nm, while another device was almost, but not fully proximized. Next, we look at some wider devices.

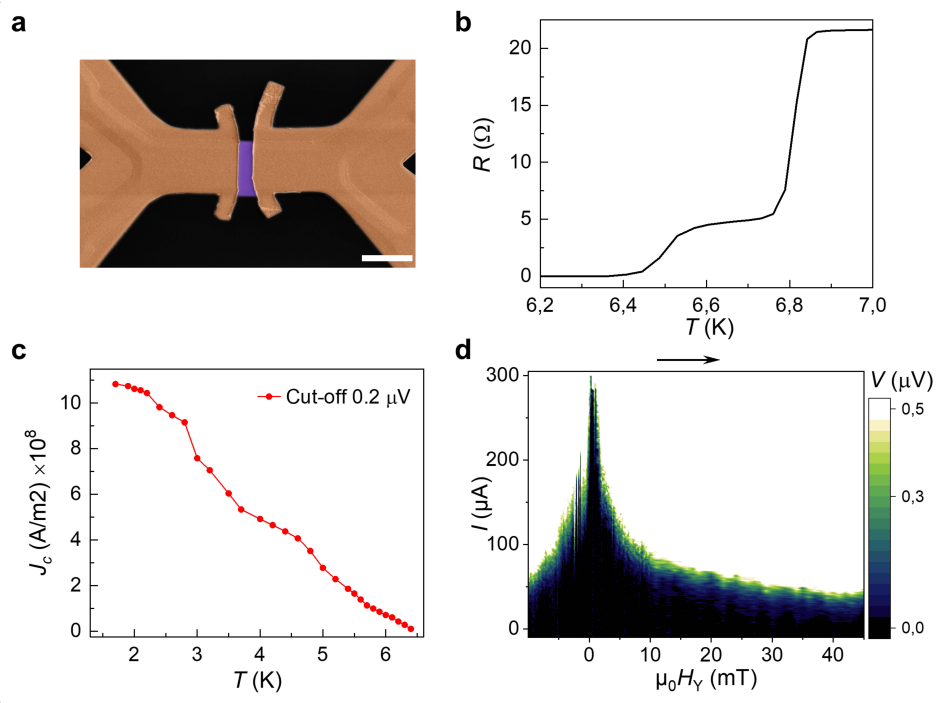

Figure 6.6: Electrical transport characterization of Dv4. (a) False-colored SEM image of Dv4. The scale bar is 5 μm. (b) A plot of the RT curve. (c) A plot of the temperature-dependent density of critical current J_c extracted by taking a criterion 0.2 μV. (d) SQI pattern obtained at 6.3 K by sweeping $B_\perp$. The arrow indicates the field sweep direction.

Devices with larger width, 5 μm

Next we study the wide junction Dv4 with 1.35 μm length and 5.12 μm width, as shown in Fig. 6.6a. Changing the dimension of the junction may give different magnetic structures, and thus may affect the LRP effect. The RT curve of Dv4 was measured

and plotted in Fig. 6.6b. Again, the resistance of Dv4 decreases to zero after two transitions. The first transition corresponds to the superconducting NbTi, leaving a residual resistance of 6 Ω. If we roughly take $\rho \approx 80$ $\mu\Omega$cm (appropriate for this width), $R_4 \approx 5.3$ Ω, meaning Dv4 is over-etched in a more or less optimal way. The second transition signifies the onset of the superconductivity in the weak link, indicating Dv4 is fully proximized. However, the temperature transition window is about 0.5 K, which is much smaller than those of Dv3 and Dv2. Also, it should be noted Dv4 is 1.349 μm long. Since Dv2 ($l \approx 678$ nm) was not fully superconducting, the observed superconductivity in Dv4 needs to be thoroughly inspected. The behavior of J_c versus temperature of Dv4 was measured as summarised in Fig. 6.6c by taking a criterion of 0.2 μV. At the base temperature (1.5 K), J_c is about 11×10^8 A/m^2, so two times larger than the measured J_c of Dv3. It is slightly surprising that the value for Dv4 is similar to, and even larger than, that of Dv3, given the fact that the junction is more than twice as long. On the other hand, such a long length is not inconceivable. Sanchez-Manzano, *et al.* reported the LRP effect in very wide YBCO/LSMO junctions (20 and 25 μm), with a length of about 1 μm, although with much lower critical currents [14].
To further confirm the Josephson coupling in Dv4, we examined the SQI pattern of Dv4 at 6.3 K by sweeping $B_\perp$ (Fig. 6.6d). The central peak of the SQI pattern is quite narrow, which is not abnormal in view of the dimension of Dv4. We estimate the expected period based on $\Delta B = \Phi_0/(wL)$, yielding $\Delta B \approx 0.3$ mT. Similar to Dv3, we see that the expected period is very small (actually smaller than can be easily measured), but that the measured pattern is wider and falls off more slowly.

We also examined Dv6 with a length of 639.8 nm and a width of 5.134 μm, as shown in Fig. 6.7a. Approximating $\rho \approx 80$ $\mu\Omega$cm (the same value as used for Dv4), R_6 is calculated to be 2.5 Ω. The measured normal resistance of Dv6 is 4.9 Ω (inset in Fig. 6.7b), suggesting Dv6 is etched as expected, meaning slightly over-etched. The SQI pattern of Dv6 was measured at 5.6 K by sweeping $B_\perp$, as displayed in Fig. 6.7b. As the effective area of Dv6 is smaller than that of Dv4, we hence see a wider central peak of the SQI pattern compared to that of Dv4, *i.e.* ΔB of Dv6 is larger. There is also a shift of the maximum I_c, which is found at -5 mT. This may be due to the misalignment between the sample and the applied field, while the glitches in the SQI pattern are possibly attributed to the microscopic structure of the disordered magnetic moments of Dv6. A more quantitative description has not been made yet [65–67].

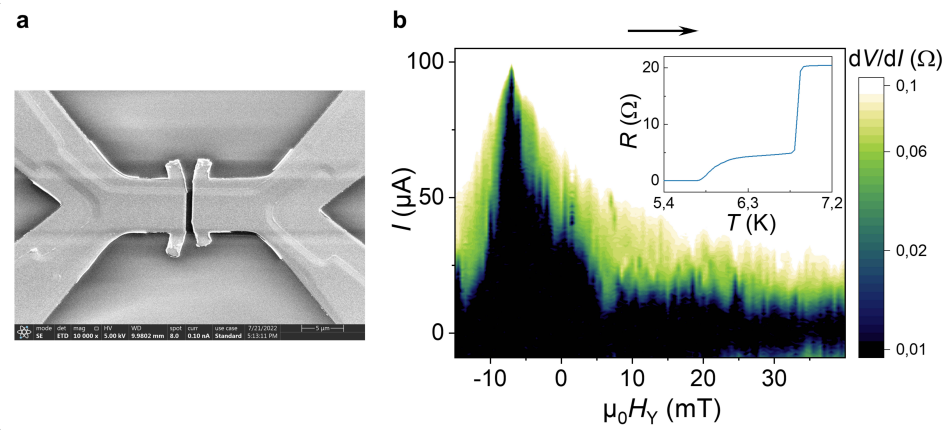

Figure 6.7: Electrical transport characterization of Dv6. (a) Top-view SEM image of Dv6. (b) SQI pattern measured at 5.6 K by sweeping $B_\perp$. The arrow indicates the field sweep direction. Inset: RT curve of Dv6.

Overview of the long NbTi/LSMO junctions

Eventually, we summarize all the calculated and measured data of the long NbTi/LSMO Devices in Table 6.2.

Junctions	l(nm)	w(μm)	R_N(Ω)	T_c(K)	TTW(K)	ΔB(mT)	J_c(A/m^2) @2K
Dv2	678	1.912	20	<0.4	>6.17	1.54	-
Dv3	585.9	2.035	20	5.19	1.54	1.68	5.09×10^8
Dv4	1349	5.118	6	6.4	0.36	0.29	10.83×10^8
Dv5	755.6	4.887	4.6	6.4	0.36	0.54	-
Dv6	639.8	5.134	4.9	5.78	0.99	0.61	-

Table 6.2: Summary of the information of the NbTi/LSMO devices. The transition window (TTW) is defined as the temperature decreases from R_N to 0, *i.e.* the establishment of the LRP in the LSMO weak link. ΔB was calculated according to $\Delta B\,w\,l = \Phi_0$.

6.4. Summary

Following up on the results of Chapter 5, and in particular on the finding that a triplet generator exists at the interface between LSMO and NbTi, we developed a lithography process to fabricate longer Josephson junctions. The process starts with bilayer films and involves using a hard mask of Pt, and a series of lithography steps. One crucial step is the removal of the 60 nm NbTi layer on the LSMO bridge. By slightly overetching, this appears feasible. We fabricated devices with different lengths and widths of the LSMO

bridge and found supercurrents in all but one, indicating that the same triplet generator is at work that we found in the devices that were fabricated by Focused Ion Beam in Chapter 5. Two devices stand out in that they could be characterized both through SQI measurements, and by measuring the temperature dependence of the critical current. One (Dv3) has a length of about 600 nm, a critical current at 2 K of 5.1 $\times 10^8$ [A/m^2], and a Gaussian-shaped SQI pattern with a width of about 15 mT. Together with the fact that the resistance of the bridge indicates slight overetching, we conclude that this is a proximized bridge, with triplet supercurrents flowing through the LSMO, and not a residual NbTi short. The other one (Dv4) is much longer (about 1.3 μm) but shows basically the same characteristics. The question still to be answered is whether the larger width of this device is (part of) the reason that the supercurrent density at 2 K is even larger than in Dv3. That would open the way to producing spin torque effects and manipulating local spins or even moving domain walls without Joule heating, giving rise to actual applications in superconducting spintronics.

6.5. Appendix

Here we summarize details of the etch process and give the etching rates that we found and used in step IV (removing the Pt mask from the full structure), and step VI (removing the NbTi on top of the LSMO bridge). Thicknesses, etch rates, and etch times are given in Table 6.3.

	Step IV			Step VI	
	thickness(nm)	etch rate(nm/min)	etch time(min)	thickness	etch time(min)
Pt	425.8	25.9	16.5	255.5	8~9
NbTi	60	7.5	~0	60	8~9
LSMO	40	6.67	~0	40	~0

Table 6.3: Overview of experimental parameters in steps IV and VI in the nanofabrication process. The thickness of the Pt mask is adapted to the different etching requirements.

$w(\mu m)$	$l(\mu m)$	$\rho(\mu\Omega cm)$
0.663	4.295	690
1.345	1.382	447
1.554	2.094	210
2.094	6.347	107
3.014	6.074	108

Table 6.4: Overview of the resistivity of the LSMO nanowires with varying widths. Here w is the width of the LSMO nanowire, and l is the distance between the voltage probes. All LSMO nanowires have an identical length of 30 μm.

The etch rates were determined by using atomic force microscopy (AFM). First, we grow Pt or NbTi on a Si substrate. Then, an electron beam resist mask is fabricated on the Pt or NbTi film. After exposing to the ion beam in the etcher for 3 min, the sample is immersed in a resist remover to dissolve the resist mask completely. As a result, a height difference between the area covered by the resist mask and the uncovered area is obtained and measured by AFM, yielding the average etching rate. Ideally, etching the sample for a long time would give a more accurate etching rate. However, the resist mask can only survive for several minutes in the etcher. We take this problem into consideration and hence always do over-etching a bit in the nanofabrication process. The etch rate of LSMO is determined using the same method. The thickness of Pt (NbTi) is measured by AFM with the help of electron beam lithography. In the case of LSMO, a thin LSMO film is fabricated, and its thickness is measured by X-ray reflectivity. An average deposition rate of LSMO can be acquired and instructs us to

grow LSMO films with the desired thickness.

We summarize the measured resistivity of LSMO nanowires (in a four-probe configuration) at 10 K in Table 6.4. As the width of LSMO nanowires becomes smaller, the resistivity becomes larger. Therefore, we use different values of resistivity to calculate the resistance of the long NbTi/LSMO junctions. The resistivity of the LSMO nanowire with a width of ~ 5 μm is approximated to be 80~100 $\mu\Omega$cm. The measured resistivity of an unstructured LSMO thin film is about 40 $\mu\Omega$cm.